10

Novel Mechanochemical Process for Aqueous - Phase Synthesis of Superparamagnetic Magnetite Nanoparticles

Tomohiro Iwasaki
Department of Chemical Engineering,
Osaka Prefecture University
Japan

1. Introduction

Nano-sized magnetite (Fe_3O_4) powder has been widely used in various industrial products: for instance, pigments, recording materials, printing and electrophotography such as copying toner and carrier powders, etc. (Buxbaum & Pfaff, 2005; Hakata, 2002; Ochiai et al., 1994) because of the excellent physicochemical properties. In particular, Fe_3O_4 nanoparticles with a size of smaller than about 20 nm exhibit a unique magnetic property, namely, superparamagnetism. In recent years, its non-toxicity property and high chemical stability have attracted much attention, and the use of superparamagnetic Fe_3O_4 nanoparticles have rapidly expanded in biomedical fields, such as magnetic resonance imaging (Hu et al., 2010; Lee et al., 2009), drug delivery (Guo et al., 2009; Zhou et al., 2009), hyperthermia (Gao et al., 2010; Muzquiz-Ramos et al., 2010), immobilization of enzymes (Wang et al., 2008) and proteins (Can et al., 2009), and magnetic separation of cells (Li et al., 2009).

For industrial production of superparamagnetic Fe_3O_4 nanoparticles, chemical coprecipitation is often employed (Buyukhatipoglu et al., 2009; Compeán-Jasso et al., 2008; Iwasaki et al., 2011a; Mizutani et al., 2010; Yang et al., 2009; Yu et al., 2010). In coprecipitation methods, ferrous and ferric ions are simultaneously precipitated as ferrous hydroxide ($Fe(OH)_2$) and goethite (α-FeOOH) in an alkaline solution, respectively, resulting in the formation of Fe_3O_4. In order to prepare superparamagnetic Fe_3O_4 nanoparticles with good dispersibility, not only the primary size of Fe_3O_4 nanoparticles must be controlled but also the aggregation of Fe_3O_4 nanoparticles must be avoided. Thus, anti-aggregation agents (e.g., surfactant) and toxic organic solvents are added to the staring solution in many cases (Cheng et al., 2005; Ge et al., 2007; Hua et al., 2008; Wan et al., 2007; Wen et al., 2008). Therefore, the Fe_3O_4 suspensions thus obtained should be washed enough before its use in the applications. In addition, for improving the crystallinity, heating treatments such as annealing and hydrothermal treatment are often performed, leading to the enhancement of the ferromagnetism (Mizutani et al., 2008; Wu et al., 2007, 2008; Zheng et al., 2006). Unfortunately, these required treatments complicate the preparation process and may increase the environmental impact and the production cost.

In order to overcome these problems, a novel synthesis method using a mechanochemical effect has been developed for the production of superparamagnetic Fe_3O_4 nanoparticles with

high crystallinity without using any environmental-unfriendly additives (Iwasaki et al., 2008, 2009, 2010, 2011b). This chapter describes the outline of this method and the kinetic analysis of the mechanochemical process.

2. Mechanochemical synthesis of Fe_3O_4 nanoparticles via coprecipitation

In this method, a tumbling ball mill is used as a reactor, and a suspension of $Fe(OH)_2$ and α-FeOOH as a precursor, which is prepared via coprecipitation, is ball-milled in an organic solvent-free water system. The ball-milling treatment is performed under a cooling condition. Thus, high mechanical energy generated by collision of ball media is applied to the precursor instead of the heat energy, which promotes the solid phase reaction between $Fe(OH)_2$ and α-FeOOH forming Fe_3O_4 and the crystallization process without the crystal growth caused by the heat energy. This corresponds to the mechanochemical effect. Accordingly, this method does not need any additional heating treatment to improve the crystallinity of the product. In addition, any additives such as surfactants and oxidizing and reducing agents are not required. Consequently, this method provides successfully superparamagnetic Fe_3O_4 nanocrystals with a size of less than 15 nm. The details of this method are described below.

Typically, 1.5 mmol of ferrous sulfate heptahydrate ($FeSO_4 \cdot 7H_2O$) and 3.0 mmol of ferric chloride hexahydrate ($FeCl_3 \cdot 6H_2O$) are dissolved in 60 ml of deionized and deoxygenated water in a beaker. The molar ratio of ferrous ion to ferric ion is 0.5, corresponding to the chemical stoichiometric ratio of the Fe_3O_4 formation reaction. 30 ml of 1.0 kmol/m^3 sodium hydroxide (NaOH) solution is added into the acid solution at a constant addition rate of 3 ml/min under vigorous stirring using a magnetic stirrer in an argon atmosphere. As the pH of the solution increased, $Fe(OH)_2$ and α-FeOOH coprecipitate, according to Eqs. (1) to (3).

$$Fe^{2+} + 2OH^- \rightarrow Fe(OH)_2 \quad (1)$$

$$Fe^{3+} + 3OH^- \rightarrow Fe(OH)_3 \quad (2)$$

$$Fe(OH)_3 \rightarrow \alpha\text{-}FeOOH + H_2O \quad (3)$$

When adding the NaOH solution, the solution temperature is kept below 5°C by ice-cooling in order to avoid the solid phase reaction forming Fe_3O_4 from $Fe(OH)_2$ and α-FeOOH according to Eq. (4) (Lian et al., 2004).

$$Fe(OH)_2 + 2\alpha\text{-}FeOOH \rightarrow Fe_3O_4 + 2H_2O \quad (4)$$

However, even under cooling, $Fe(OH)_2$ and α-FeOOH partially take place the Fe_3O_4 formation reaction. This results in a dark brown suspension with a pH of higher than 12 containing $Fe(OH)_2$, α-FeOOH, and a tiny amount of Fe_3O_4. The suspension thus prepared is subjected to the following ball-milling treatment.

The starting suspension is poured into a milling pot with an inner diameter of 90 mm and a capacity of 500 ml, made of stainless steel (18%Cr-8%Ni). Stainless steel balls with a diameter of 3.2 mm are used as the milling media. The charged volume of balls containing the void formed among them is 40% of the pot capacity, as illustrated in Fig. 1.

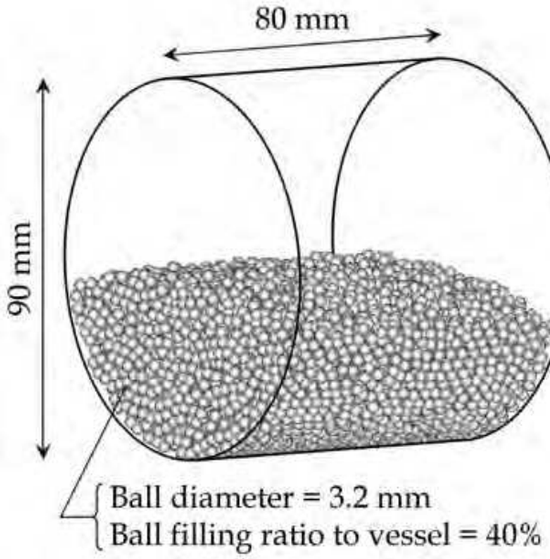

Fig. 1. Schematic illustration of tumbling ball mill used in this work.

After replacement of air in the milling pot with argon, the milling pot is sealed. In order to promote the reaction between $Fe(OH)_2$ and α-FeOOH, the ball-milling treatment is then carried out by rotating the milling pot at rotational speeds of 35 to 140 rpm (corresponding to 16% to 64% of the critical rotational speed (= 220 rpm) determined experimentally based on the behavior of balls containing the suspension) for a given time. During the ball-milling treatment, the milling pot is cooled from its outside in a water bath. Temperature of the water bath is kept at 1.0±0.1°C, and temperature of the suspension is between 1.6°C and 1.7°C within the rotational speed range; this means that the milling pot is cooled enough. After the ball-milling treatment, the obtained precipitate is washed and then dried at 30°C under vacuum overnight.

The dried samples thus obtained were characterized according to standard methods. The powder X-ray diffraction (XRD) pattern of samples was measured with CuKα radiation ranging from 2θ = 10 to 80° at a scanning rate of 1.0°/min using a Rigaku RINT-1500 powder X-ray diffractometer. Fig. 2 shows the XRD pattern of samples obtained at various rotational speeds of the milling pot. In all the XRD patterns, clear diffractions indicating $Fe(OH)_2$ phase were not observed because it tends to form amorphous phase. Before the ball-milling treatment, the sample contained amorphous α-FeOOH and Fe_3O_4 phases. As the milling time elapsed, α-FeOOH gradually disappeared and finally the single-phase of Fe_3O_4 formed. This reaction can be attributed to the application of the mechanical energy generated by collision of the balls to α-FeOOH and $Fe(OH)_2$. The reaction rate depended strongly on the rotational speed. The time required for completing the Fe_3O_4 formation reaction was reduced with increasing in the rotational speed; the reaction almost completed in 12 h at 35 rpm, in 9 h at 70 rpm, in 7.5 h at 105 rpm, and in 6 h at 140 rpm. On the other hand, when the ball-milling treatment was not conducted, i.e., the suspension was kept cooling statically at below 2°C in the water bath, the XRD pattern was almost the same as that of the staring precipitate even after 12 h. It was confirmed that the ball-milling treatment promoted the solid phase reaction by the mechanochemical effect. At early stages of the ball-milling treatment, α-FeOOH seemed to increase from the initial. Actually,

suspensions at early stages had light brown colors as compared to the staring suspension. This implies that $Fe(OH)_2$ is oxidized and Fe_3O_4 is decomposed (hydrolyzed) because $Fe(OH)_2$ and Fe_3O_4 in the starting solution are relatively unstable. As the milling time elapsed, the color of the suspension became darker brown, and finally black precipitates were obtained. This result also implies the reduction of α-FeOOH. Fe_3O_4 formed by the mechanical energy is hardly decomposed during ball-milling because it is well crystallized and becomes stable.

The samples had the typical diffraction angles showing relatively high peaks, agreed well with those of Fe_3O_4 phase. The average crystallite size was calculated from the full-width at half-maximum (FWHM) of the Fe_3O_4 (311) diffraction peak at $2\theta \approx 35.5°$ using the Scherrer's formula. The lattice constant was also determined from several diffraction angles showing high intensity peaks. The lattice constant was determined to be between 8.374 and 8.395 Å and close to the standard value of Fe_3O_4 (= 8.396 Å) rather than γ-Fe_2O_3 (= 8.345 Å). These results support that the samples had a single Fe_3O_4 phase rather than γ-Fe_2O_3 regardless of the milling conditions.

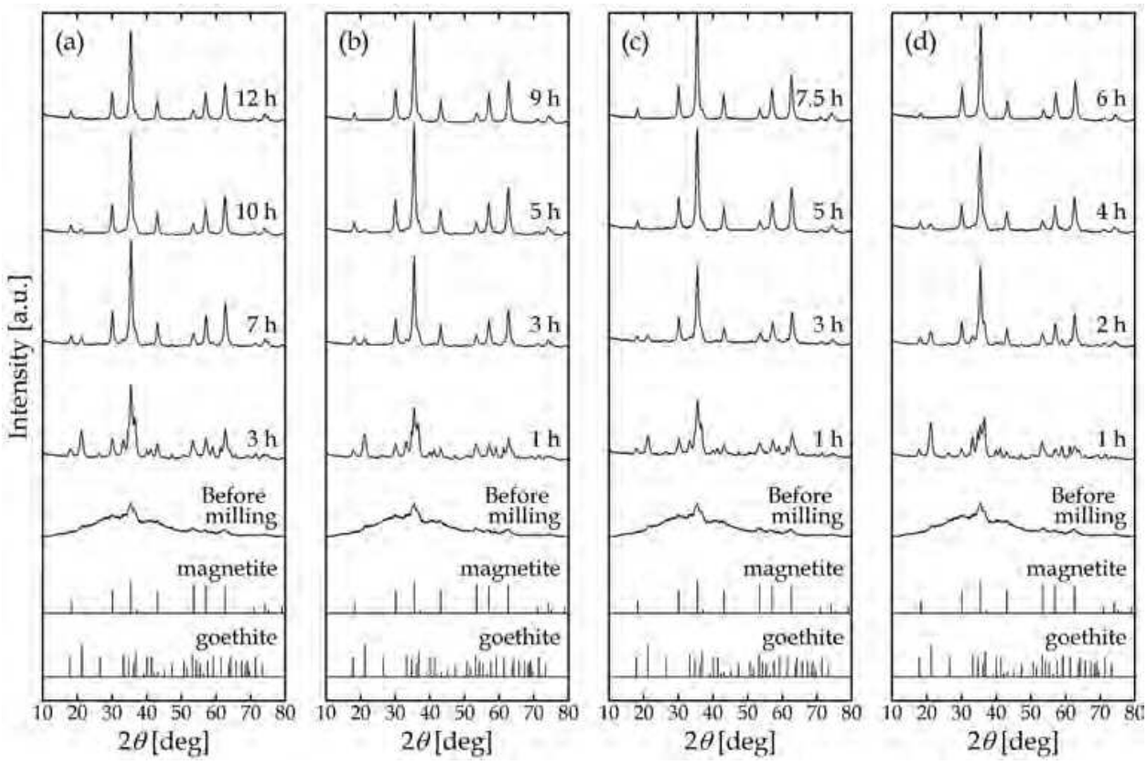

Fig. 2. XRD pattern of samples obtained at (a) 35, (b) 70, (c) 105, and (d) 140 rpm.

The morphology of samples was observed with a field emission scanning electron microscope (FE-SEM; JSM-6700F, JEOL). Fig. 3 shows the SEM image of samples. The samples were spherical nanoparticles with a size of about 10–20 nm.

The hydrodynamic particle size distribution of samples was measured by dynamic light scattering (DLS-700, Otsuka Electronics) for the sample-redispersed aqueous suspension containing a small amount of sodium dodecyl sulphate as a dispersion stabilizer. The

median diameter (number basis) was determined from the obtained size distribution. Fig. 4 indicates the particle size distribution of samples. The samples had a narrow size distribution with a median diameter of about 11 nm. The median size almost agreed with the average crystallite size and the particle size observed by SEM; this means that the crystallinity of samples was high.

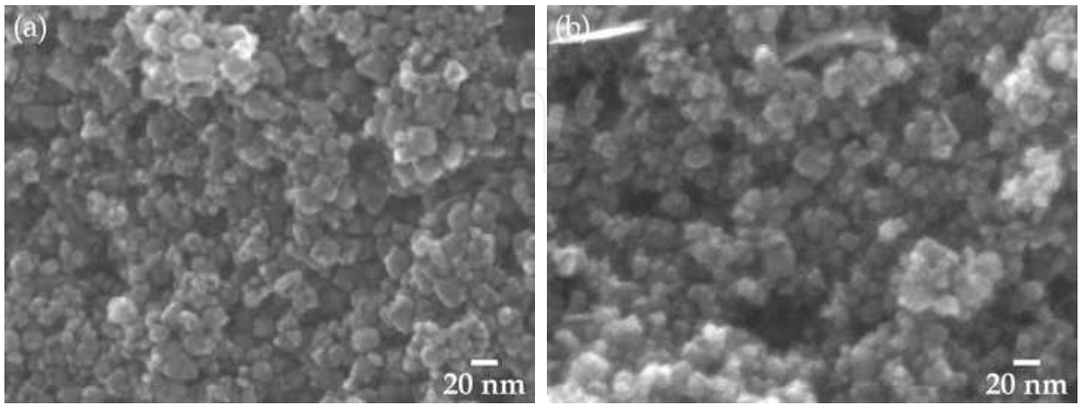

Fig. 3. SEM images of samples obtained (a) at 35 rpm in 12 h and (b) at 140 rpm in 6 h.

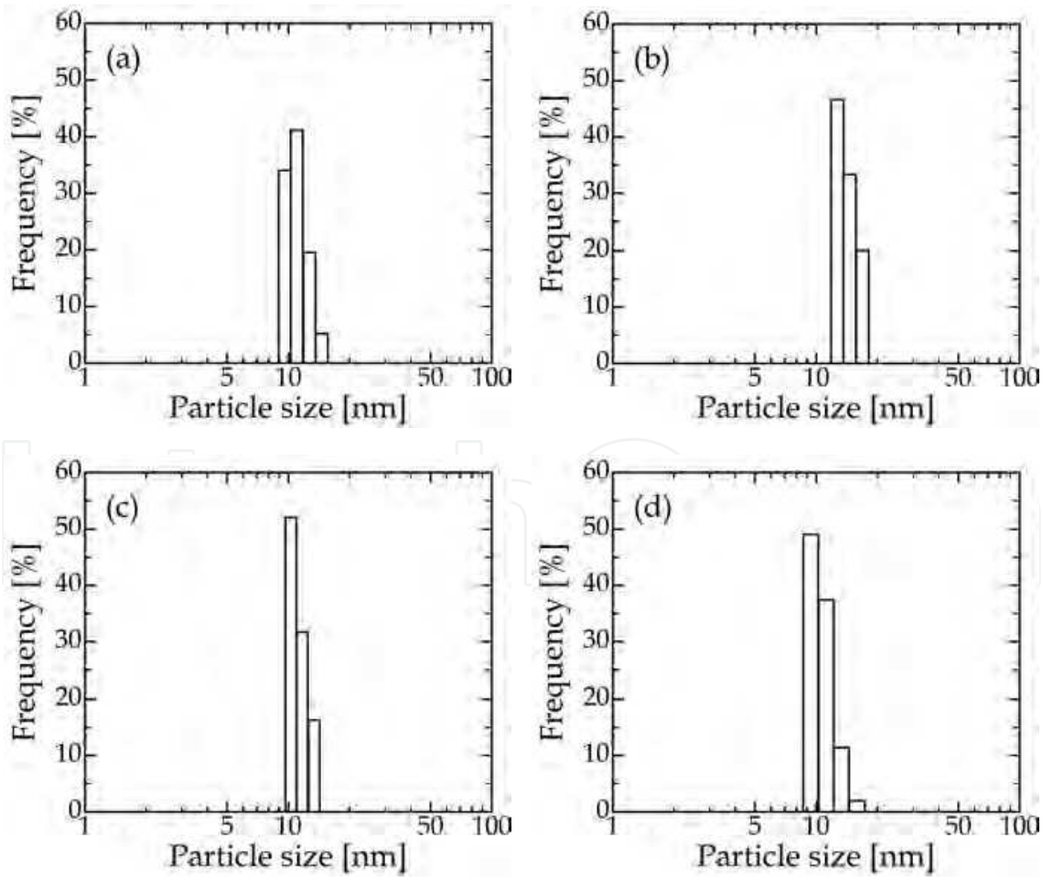

Fig. 4. Particle size distribution of samples obtained (a) at 35 rpm in 12 h, (b) at 70 rpm in 9 h, (c) at 105 rpm in 7.5 h, and (d) at 140 rpm in 6 h.

The magnetic property (magnetization-magnetic field hysteretic cycle) was analyzed using a superconducting quantum interference device (SQUID) magnetometer (Quantum Design model MPMS) at room temperature in the rage of magnetic field between –10 kOe and 10 kOe. Fig. 5 shows the magnetization-magnetic field curve of samples. The samples had a low coercivity, showing superparamagnetism. The saturation magnetization was a little lower than that of the corresponding bulk (= 92 emu/g) because of the smaller size (Lee et al., 1996).

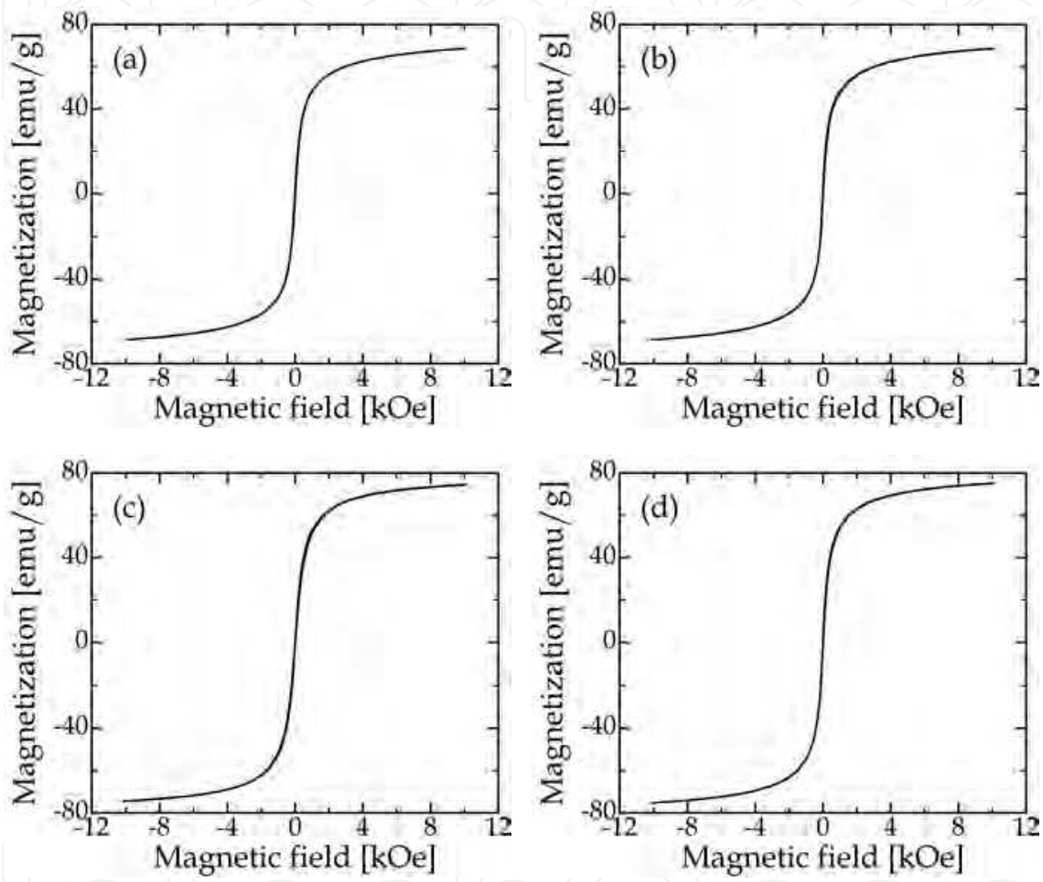

Fig. 5. Magnetization-magnetic field curve of samples obtained (a) at 35 rpm in 12 h, (b) at 70 rpm in 9 h, (c) at 105 rpm in 7.5 h, and (d) at 140 rpm in 6 h.

Table 1 summarizes the properties. The zeta potential was measured with a zeta potential analyzer (Zetasizer Nano ZS, Malvern Instruments). As can be seen in Table 1, the Fe_3O_4 nanoparticles with similar properties were obtained regardless of the rotational speed. The zeta potential of samples was relatively high with adding neither anti-aggregation agents nor organic solvents in the synthesis and almost the same even when the mechanical energy applied to the suspension per unit time was varied. This reveals that the applied mechanical energy hardly affected the dispersibility of Fe_3O_4 nanoparticles.

In this method, the sample contamination caused by the wear of milling pot and balls is concerned. Therefore, the chemical component of samples was determined by means of an energy dispersive X-ray spectrometer (EDS; JED-2300F, JEOL) equipped with the FE-SEM.

Table 2 gives the impurity content in the samples. The sample contamination had a tendency to increase at higher rotational speeds. However, the use of fluorocarbon resin-lined pot and carbon steel balls can decrease the incorporation of Cr and Ni into the product even at higher rotational speeds.

Milling conditions				
Rotational speed [rpm]	35	70	105	140
Milling time [h]	12	9	7.5	6
Average crystallite size [nm]	11.2	11.3	10.8	11.9
Lattice constant [Å]	8.395	8.385	8.392	8.374
Median size [nm]	9.5	10.9	10.3	8.8
Saturation magnetization [emu/g]	68.7	68.6	74.6	75.2
Coercivity [Oe]	9	7	2	1
Zeta potential [mV]	–16.3	–15.6	–20.6	–18.1

Table 1. Properties of samples obtained under various conditions.

Milling conditions				
Rotational speed [rpm]	35	70	105	140
Milling time [h]	12	9	7.5	6
Cr [wt.%]	0.39	0.62	1.26	1.21
Ni [wt.%]	0.10	0.37	0.61	0.69
Na [wt.%]	0.53	0.19	0.25	0.32
S [wt.%]	0.08	0.03	0.03	0.03
Cl [wt.%]	0.15	0.02	0.02	0.04

Table 2. Impurity content in samples.

Generally, preparation of nanoparticles with a size of less than 20 nm is very difficult by means of grinding techniques using ball mills and bead mills (i.e., break-down methods) even under wet conditions. In particular, tumbling mills are impossible to provide such nanoparticles by grinding because the mechanical energy generated in tumbling mills is too low to reach a particle size less than several micrometers. Accordingly, the mechanical energy is used not for the grinding of coarse (grown) particles but for the Fe_3O_4 formation reaction; the Fe_3O_4 nanoparticles are prepared by means of a build-up method. Consequently, the obtained results shown above demonstrate that this synthesis method is effective for the production of superparamagnetic Fe_3O_4 nanoparticles with good dispersibility.

3. Analysis of mechanochemical process

3.1 Reaction rate equation in mechanochemical process

For kinetically analyzing this mechanochemical process, the reaction rate equation must be derived. Therefore, the change in the concentration of the starting materials with the reaction time is required. In this investigation, the concentration of the starting materials was approximately estimated from the XRD data. As mentioned earlier, in this mechanochemical process, the formation and conversion of α-FeOOH plays an important

role rather than $Fe(OH)_2$. Accordingly, the temporal change in the content of α-FeOOH in the product was focused on. In order to estimate the content of α-FeOOH from the XRD data, the relationship between the content of α-FeOOH and the diffraction intensity is needed as an analytical curve. Therefore, virtual products with various compositions of α-FeOOH and Fe_3O_4, expressed by the molar ratio γ of α-FeOOH to the α-FeOOH–Fe_3O_4 mixture, were artificially prepared by mixing appropriate amounts of α-FeOOH and Fe_3O_4. The XRD analysis for the virtual products was conducted, and the diffraction intensity I at $2\theta = 21.2°$ corresponding to the (011) plane of α-FeOOH was measured. The intensity ratio ξ was calculated, defined by

$$\xi = (I - I_m)/(I_g - I_m) \quad (5)$$

where I_g and I_m indicate the peak intensity at $2\theta = 21.2°$ for α-FeOOH and Fe_3O_4, respectively. Fig. 6 shows the intensity ratio ξ as a function of the molar ratio γ. Using this analytical curve, the concentration C_g of α-FeOOH in the suspension was estimated.

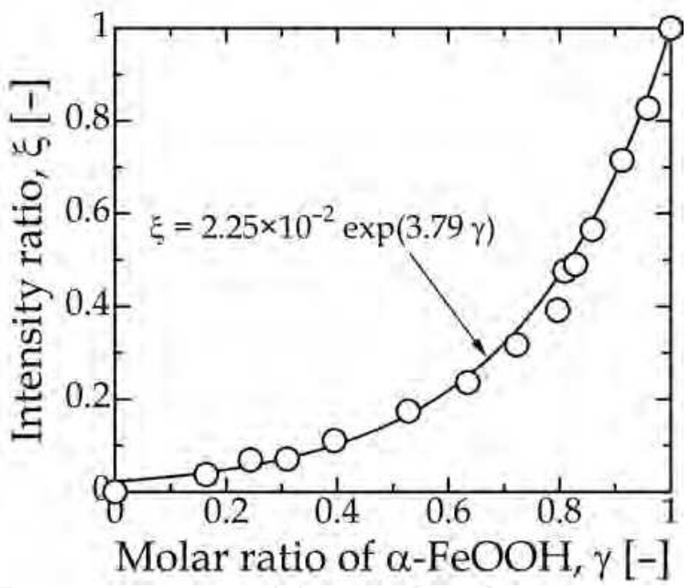

Fig. 6. Relationship between intensity ratio ξ and molar ratio γ of α-FeOOH.

Fig. 7 shows the change in C_g with the milling time t_m at the rotational speed of 140 rpm as an example. C_g increased immediately after the ball-milling treatment began and then decreased with the milling time. The similar tendency was observed at other rotational speeds. The highest C_g observed in 1800 s almost agreed with the concentration of total iron in the starting solution (≈ 4.5 mmol/90 ml = 50 mol/m^3). This implies that the total iron in the starting solution may be converted to α-FeOOH at an initial stage of the ball-milling treatment, and after that, Fe_3O_4 may form from α-FeOOH by the mechanochemical effect. Thus, the formation path of Fe_3O_4 in this mechanochemical process can differ from that in conventional coprecipitation processes.

From these results shown above, a possible reaction mechanism of Fe_3O_4 formation can be constructed as follows. At an initial stage of the ball-milling treatment, amorphous phases of $Fe(OH)_2$ and Fe_3O_4 in the staring suspension are rapidly oxidized and hydrolyzed by the

mechanochemical effect according to Eqs. (6) and (7), respectively, resulting to the formation of single α-FeOOH phase.

$$Fe(OH)_2 \rightarrow \alpha\text{-}FeOOH + \tfrac{1}{2}H_2 \quad (6)$$

$$Fe_3O_4 + 2H_2O \rightarrow 2\alpha\text{-}FeOOH + Fe(OH)_2 \quad (7)$$

After that, α-FeOOH is partially reduced to $Fe(OH)_2$ by the generated H_2 gas, and the formed $Fe(OH)_2$ reacts immediately with α-FeOOH, resulting to the formation of Fe_3O_4.

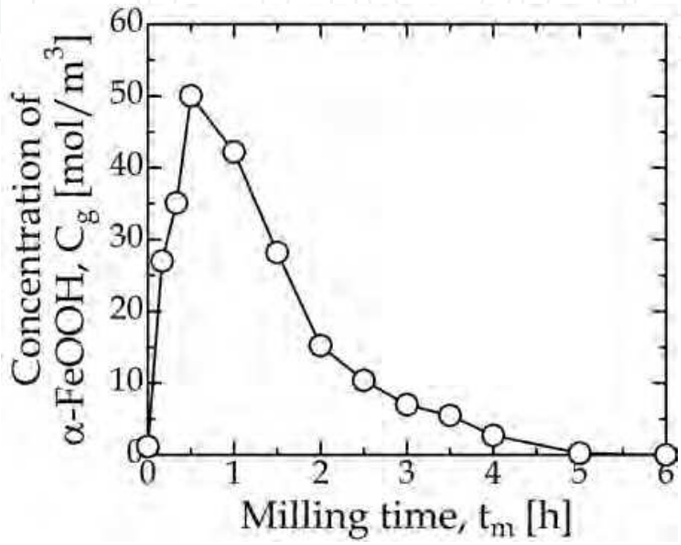

Fig. 7. Change in concentration C_g of α-FeOOH with milling time t_m at rotational speed of 140 rpm.

$$\alpha\text{-}FeOOH + \tfrac{1}{2}H_2 \rightarrow Fe(OH)_2 \quad (8)$$

$$2\alpha\text{-}FeOOH + Fe(OH)_2 \rightarrow Fe_3O_4 + 2H_2O \quad (4)$$

From these reaction equations, the overall apparent equation for the formation of Fe_3O_4 can be expressed by

$$3\alpha\text{-}FeOOH + \tfrac{1}{2}H_2 \rightarrow Fe_3O_4 + 2H_2O \quad (9)$$

Consequently, in this analysis, it can be assumed that the single α-FeOOH phase is gradually converted to Fe_3O_4 after the milling time of 1800 s according to Eq.(9). Here, the reaction time t was newly defined as

$$t = t_m - 1800 \quad (10)$$

Fig. 8 shows the change in the concentration ratio C_g/C_0 with the reaction time t, where C_0 indicates the initial concentration of α-FeOOH at t = 0. C_g/C_0 decreased exponentially with t, suggesting that the conversion reaction from α-FeOOH to Fe_3O_4 may be described by the n-th order rate equation. In this case, the reaction rate equation is expressed by

$$dC_g/dt = -kC_g^n \quad (11)$$

where k and n are the rate constant and the order of reaction, respectively. By solving this differential equation using the boundary condition, $C_g = C_0$ at t = 0, the concentration ratio C_g/C_0 is expressed by

$$C_g/C_0 = \{1+(n-1)kC_0^{n-1}t\}^{1/(1-n)} \quad (12)$$

As shown in Fig. 8, the data of the concentration of α-FeOOH against the reaction time were fitted to Eq. (12), and the values of n and k were determined. Fig. 9 shows n and k as a function of the rotational speed, respectively. n was kept almost constant, about 0.6, regardless of the rotational speed. Accordingly, the formation reaction of Fe_3O_4 expressed by Eq. (9) may be described by the 0.6th-order rate equation. On the other hand, k increased with increasing in the rotational speed. At higher rotational speeds, higher mechanical energy is generated per unit time in the ball-milling treatment. Thus, this phenomenon relating to the increase in k in this mechanochemical process is analogous to an increase in the reaction rate at higher temperatures, at which greater amounts of heat energy are given to the system.

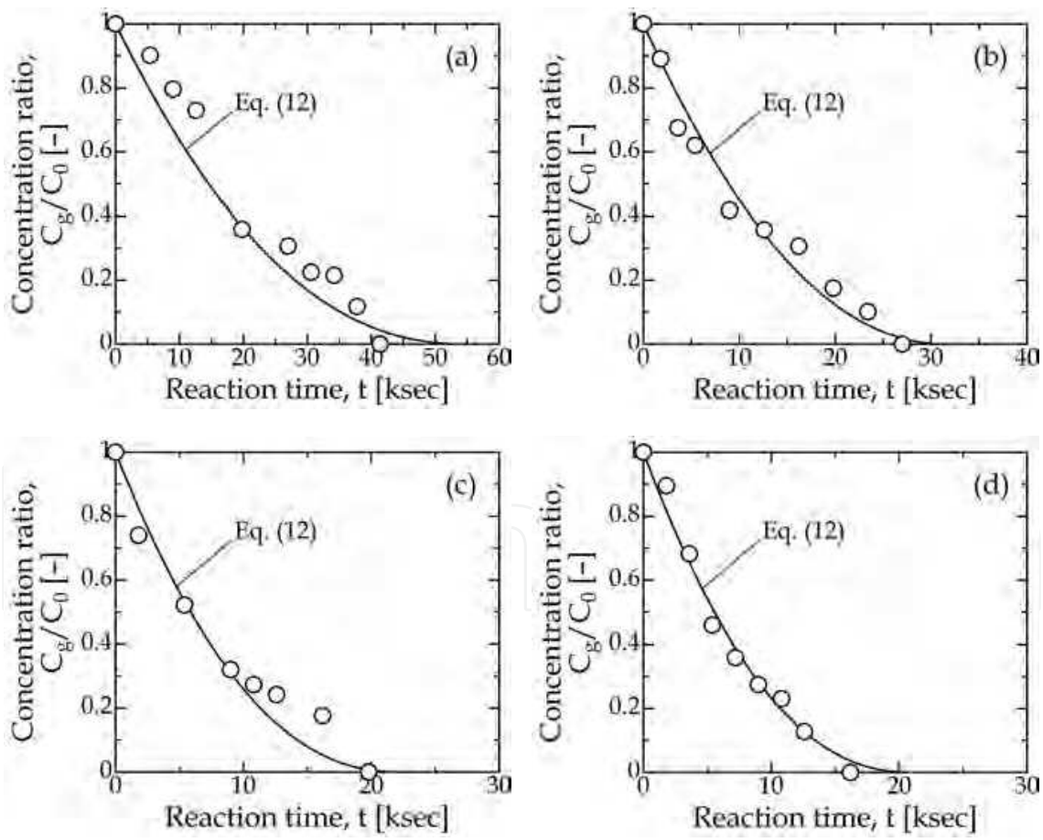

Fig. 8. Change in concentration ratio C_g/C_0 with reaction time t at rotational speeds of (a) 35 rpm, (b) 70 rpm, (c) 105 rpm, and (d) 140 rpm.

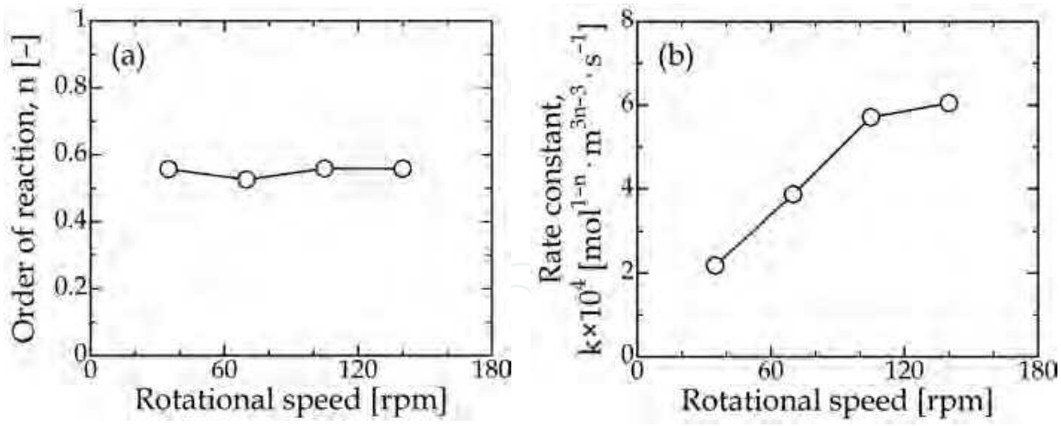

Fig. 9. Changes in (a) order of reaction n and (b) rate constant k with rotational speed.

Fig. 10 shows the effect of the initial iron concentration C_0 on the reaction rate. There was no noticeable difference among the results. Fig. 11 shows the change in n and k with C_0. n and k were almost constant against the variation in C_0. In this mechanochemical process, the order of reaction was relatively small. This means that the concentration dependence of the reaction rate is low in this system where the reaction proceeds using the mechanical energy, unlike those using the heat energy. Generally, in liquid-phase reaction processes using heating treatments, the reaction solution is heated overall and the reaction proceeds everywhere in the solution. Thus, higher concentration of staring materials tends to lead to faster reaction rate. On the other hand, in this mechanochemical process, the mechanical energy promoting the reaction is applied to the suspension on the impact points of the balls, which distribute discretely in the milling pot. Thus, even when the concentration is high, the suspension which can receive the mechanical energy is limited. This makes the effect of the initial concentration on the reaction rate small.

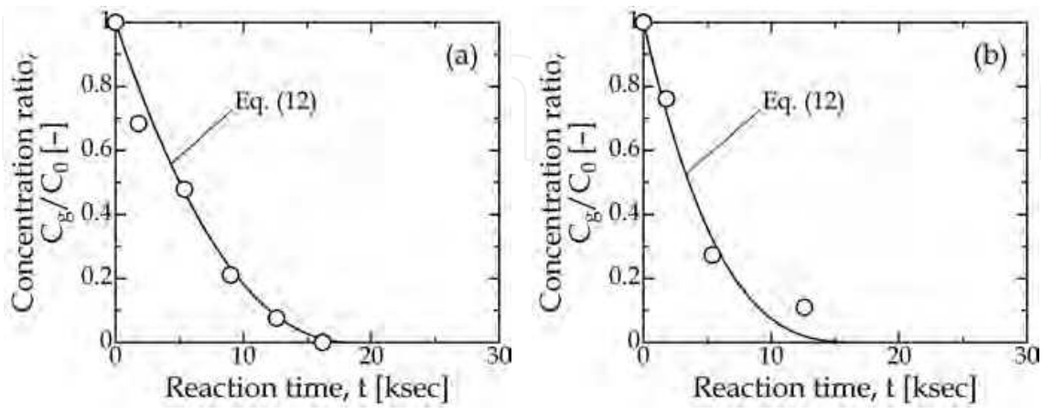

Fig. 10. Effect of initial concentration C_0 on reaction rate at 140 rpm: (a) C_0 = 25 mol/m^3 and (b) C_0 = 12.5 mol/m^3.

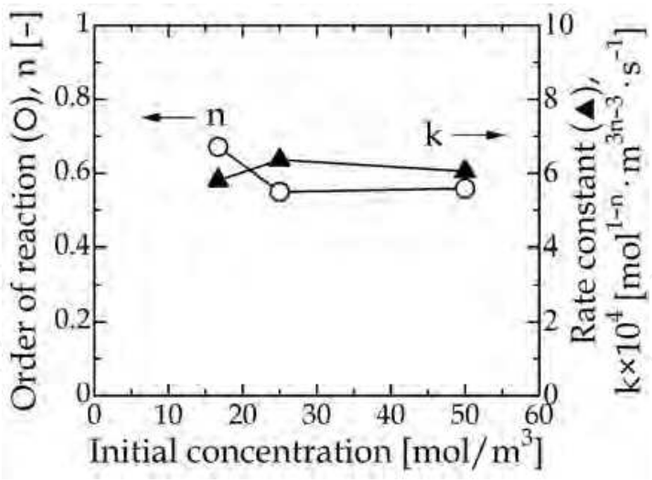

Fig. 11. Changes in n and k with initial concentration C_0.

3.2 Mechanical energy generated in mechanochemical process

In order to analyze in more details this mechanochemical process, the mechanical energy generated by collision of the balls, i.e., the impact energy of balls, was numerically analyzed by simulating the behavior of balls in the milling pot by means of the discrete element method (DEM). Based on the analysis results, the contribution of the mechanical energy to the Fe_3O_4 formation reaction was investigated, and the reaction mechanism in this system was analyzed.

For calculating the impact energy of balls, the behavior of balls in the milling pot under wet condition was simulated using the three-dimensional DEM. This simulation model describes the motion of each ball based on Newton's second law for individual ball, allowing for the external forces acting on the ball (Cundall and Strack, 1979). In this model, the interaction between ball and atmosphere gas (argon) was neglected because the contact force acting on the colliding balls is much stronger than the drag force acting on the balls in the translational motion. The fundamental equations of translational and rotational motions of a ball are expressed as follows:

$$d^2\mathbf{X}/dt^2 = (\mathbf{F}/M)+\mathbf{g} \tag{13}$$

$$d\boldsymbol{\omega}/dt = \mathbf{T}/I_b \tag{14}$$

where $\mathbf{X}$, M, $\boldsymbol{\omega}$, and I_b are mass, position, inertia moment, and angular velocity of a ball, respectively. t, $\mathbf{g}$, $\mathbf{F}$, and $\mathbf{T}$ are time, gravity acceleration, contact force, and torque caused by the tangential contact force, respectively. $\mathbf{X}$ and $\boldsymbol{\omega}$ were calculated by integrating Eqs. (13) and (14) with respect to time between t and t+Δt.

For estimating the contact force acting on a ball, the Hertz-Mindlin contact model was used. The contact forces of normal and tangential directions, $\mathbf{F}_n$ and $\mathbf{F}_t$, were estimated using the following equations:

$$\mathbf{F}_n = (-\kappa_n \boldsymbol{\delta}_n^{3/2} - \eta_n \mathbf{v}_n \cdot \mathbf{n})\mathbf{n} \tag{15}$$

$$\mathbf{F}_t = -\kappa_t \boldsymbol{\delta}_t - \eta_t \mathbf{v}_t \quad (\text{when } |\mathbf{F}_t| \leq \mu |\mathbf{F}_n|) \tag{16}$$

$$\mathbf{F}_t = -\mu |\mathbf{F}_n| (\mathbf{v}_t / |\mathbf{v}_t|) \quad (\text{when } |\mathbf{F}_t| > \mu |\mathbf{F}_n|) \tag{17}$$

$$\mathbf{v}_t = \mathbf{v} - (\mathbf{v} \cdot \mathbf{n})\mathbf{n} + r(\boldsymbol{\omega}_i + \boldsymbol{\omega}_j) \times \mathbf{n} \tag{18}$$

where $\boldsymbol{\delta}$, $\mathbf{v}$, κ, η, μ, r, and $\mathbf{n}$ are overlap displacement between contacting balls, relative velocity of contacting balls, stiffness, damping coefficient, sliding friction coefficient, radius of a ball, and unit vector of normal direction at a contact point, respectively. The subscripts n and t mean the components of normal and tangential directions at a contact point, respectively. The subscripts i and j indicate the number of contacting balls. κ and η are determined from the following equations (Tsuji et al., 1992).

Stiffness for the ball-to-ball collision:

$$\kappa_n = (2r)^{1/2} Y_b / [3(1-\sigma_b^2)] \tag{19}$$

$$\kappa_t = 2(2r)^{1/2} Y_b \boldsymbol{\delta}_n^{1/2} / [2(1+\sigma_b)(2-\sigma_b)] \tag{20}$$

Stiffness for the ball-to-pot wall collision:

$$\kappa_n = (4/3) r^{1/2} / [(1-\sigma_b^2)/Y_b + (1-\sigma_w^2)/Y_w] \tag{21}$$

$$\kappa_t = 8 r^{1/2} Y_b \boldsymbol{\delta}_n^{1/2} / [2(1+\sigma_b)(2-\sigma_b)] \tag{22}$$

Damping coefficient:

$$\eta_n = \eta_t = \alpha (M\kappa_n)^{1/2} \boldsymbol{\delta}_n^{1/4} \tag{23}$$

where Y and σ are Young's modulus and Poisson's ratio, respectively. The subscripts b and w indicate ball and pot wall, respectively. α is the constant depending on the restitution coefficient and was determined to be 0.20 based on the experimental value of restitution coefficient (= 0.75) according to the method proposed by Tsuji et al. (1992). The simulation parameters are summarized in Table 3. The sliding friction coefficient used in the calculation was determined based on the critical rotational speed measured experimentally under wet condition (Gudin et al., 2007).

The impact energy of each ball in a single collision, E_i, was defined as the kinetic energy of a ball contacting with another ball or the pot wall (Kano et al., 2000).

$$E_i = (1/2) M |\mathbf{v}|^2 \tag{24}$$

Here, $\mathbf{v}$ is the relative velocity of a ball at the moment when contacting. The ball behavior was simulated using the calculation parameters presented in Table 3, and the impact energy of balls was determined. The balls collide with each other at various relative velocities during ball-milling, resulting in the generation of various amounts of the impact energy. Thus, the impact energy of balls is distributed, as shown in Fig. 12. The distribution of the impact energy shifted to a high energy range with increasing in the rotational speed because of vigorous motion of the balls at higher rotational speeds.

Next, the impact energy of balls per unit time, E, was defined as the total kinetic energy of contacting balls.

$$E = \sum^{f} (1/2)M|\mathbf{v}|^2 \tag{25}$$

Number of balls	7218
Ball diameter	3.2 mm
Pot diameter	90 mm
Pot depth	80 mm
Ball filling ratio to pot capacity	40%
Density of ball and pot	7930 kg/m^3
Young's modulus of ball and pot	197 GPa
Poisson's ratio of ball and pot	0.30
Sliding friction coefficient	0.23
Time step	1.0 μs

Table 3. Simulation parameters used in calculations.

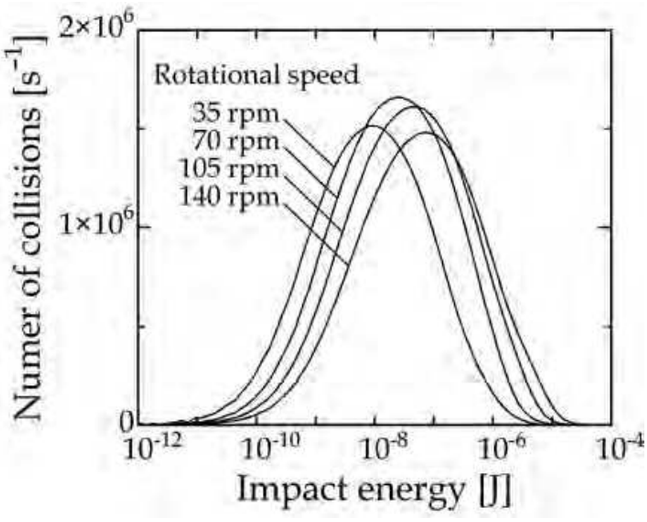

Fig. 12. Effect of rotational speed on impact energy distribution.

f is the average number of contact points per unit time. Eq.(25) means that the kinetic energy of balls just before contacting (i.e., at $|\boldsymbol{\delta}| = 0$) is summed up for all the contact points within unit time but the kinetic energy during contacting (i.e., within $|\boldsymbol{\delta}| > 0$) is not calculated. Therefore, the impact energy thus defined corresponds to the maximum kinetic energy of balls when colliding. Fig. 13 shows the calculation result of the impact energy per unit time. The impact energy was approximately proportional to the rotational speed. This implies that the impact energy depends on the number of revolutions of the pot per unit time rather than the kinetic energy of the rotational motion of the pot. The impact energy considerably varied depending on the rotational speed, resulting in variation of the milling time required for completing the Fe_3O_4 formation reaction. However, the properties of obtained Fe_3O_4 nanoparticles were almost the same even when the rotational speed was varied as shown above. This reveals that the grinding of Fe_3O_4 nanoparticles do not occur in this process and that the impact energy greatly influences the formation process of Fe_3O_4 nanoparticles (in particular, the reaction rate) rather than the properties of products.

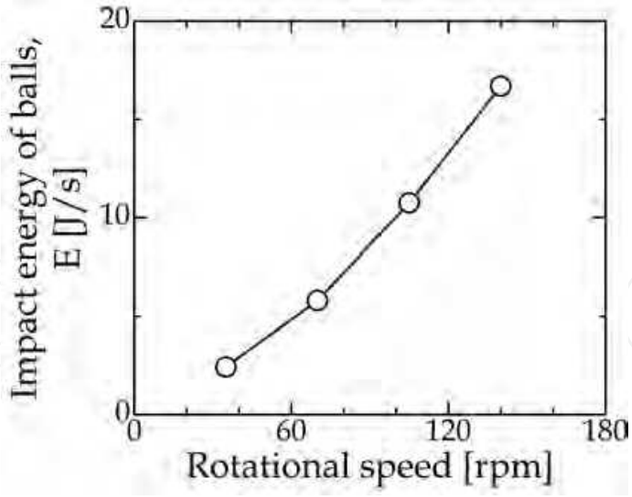

Fig. 13. Change in impact energy of balls with rotational speed.

Fig. 14 shows the relationship between the rate constant k and the impact energy E. k increased with increasing in E. This result reveals that the reaction rate increases under high mechanical energy fields. As mentioned above, this is analogous to increase of the reaction rate caused by temperature rise of the system, i.e., increase of the heat energy given to the system. As can be seen in Fig. 14, the value of k at the rotational speed of 140 rpm was not so large while relatively great amount of mechanical energy applied to the suspension. This suggests that the impact energy was not effectively used for progress of the reaction at high rotational speeds.

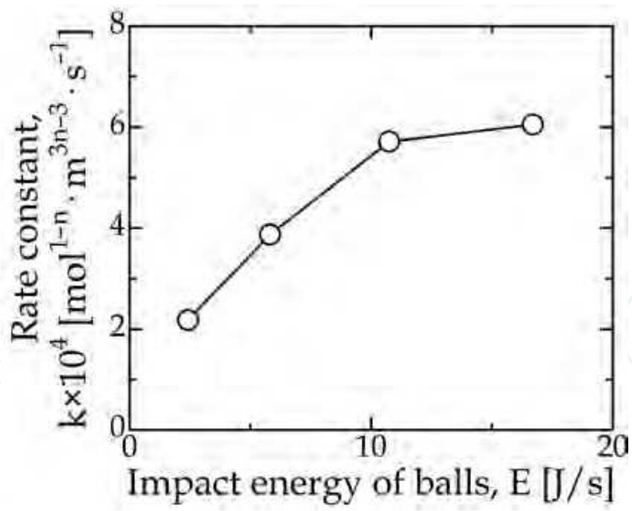

Fig. 14. Relationship between rate constant k and impact energy E of balls per unit time.

3.3 Mechanical energy required for Fe_3O_4 formation reaction

The Fe_3O_4 formation reaction can occur when the impact energy exceeding a threshold value (corresponding to the activation energy) applies to α-FeOOH at the contact points. Smaller impact energy than the threshold value cannot promote the reaction. Assuming

that the region where the impact energy applies is extremely small, even though the impact energy larger than the threshold value generates at the contact point, α-FeOOH far away from there may not react using the surplus energy. Thus, it is considered that progress of the reaction at the contact points depends on whether the impact energy exceeding the threshold value is given to α-FeOOH or not, and that the surplus energy cannot promote the reaction. Accordingly, the reaction rate can be proportional to the number of collisions that the reaction occurred. The relationship between the rate constant k and the number n_t of collisions per unit time with the energy exceeding predetermined threshold values is shown in Fig. 15. As can be seen in Fig. 15, the correlation between k and n_t was expressed by

$$k = a n_t^b \tag{26}$$

where a and b are the coefficients depending on the threshold value. Fig. 16 shows the relationship between the predetermined threshold value and the coefficient b. As indicated in Eq. (26), when b = 1, k is proportional to n_t. From Fig. 16, the threshold value giving b = 1 was determined to be 93.7 nJ. The analysis result reveals that the Fe_3O_4 formation reaction occurs at the contact points where the impact energy exceeding 93.7 nJ generates, regardless of the rotational speed. Consequently, this threshold value may be closely related to the activation energy in this reaction system. Fig. 17 shows the number of collisions per unit time that the impact energy more than 93.7 nJ generates as a function of the rotational speed. The number of collisions increased with increasing in the rotational speed.

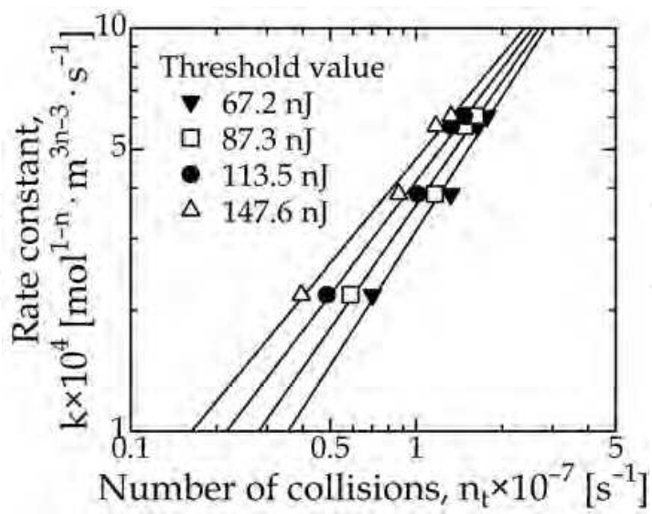

Fig. 15. Relationship between rate constant k and number n_t of collisions of balls per unit time for various threshold values of impact energy.

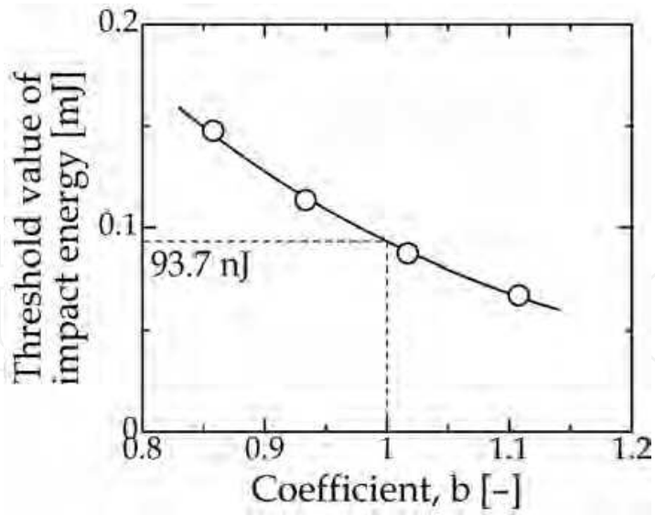

Fig. 16. Relationship between threshold value of impact energy and coefficient b.

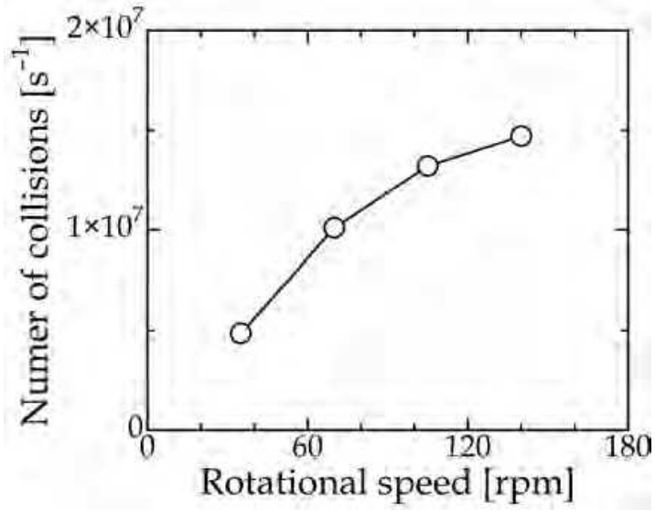

Fig. 17. Change in number of collisions generating impact energy more than 93.7 nJ with rotational speed.

This threshold value of the impact energy in a single collision, the number of collisions shown in Fig. 17, and the completion time of the Fe_3O_4 formation reaction shown in Fig. 8 were used to estimate the accumulative impact energy required for completing the Fe_3O_4 formation reaction. Fig. 18 shows the variation in the accumulative impact energy with the rotational speed. It was found that the accumulative impact energy was almost constant regardless of the rotational speed. Because the accumulative impact energy is the mechanical energy required for synthesizing 1.5 mmol of Fe_3O_4, the accumulative impact energy per 1 mol of Fe_3O_4 is defined as the apparent activation energy. Using the average of the accumulative impact energy, the apparent activation energy was determined to be 15.6 MJ/mol, which was independently of the rotational speed. This result is also analogous to the fact that generally the activation energy is independently of the reaction temperature in reaction systems using heat energy. However, the apparent activation energy thus

determined was considerably larger than the activation energy in conventional liquid-phase reaction systems because the impact energy was the maximum mechanical energy which α-FeOOH is able to receive. When both the net mechanical energy transferred from the balls to α-FeOOH and the amount of α-FeOOH receiving the energy are known, the true activation energy of the mechanochemical reaction can be determined.

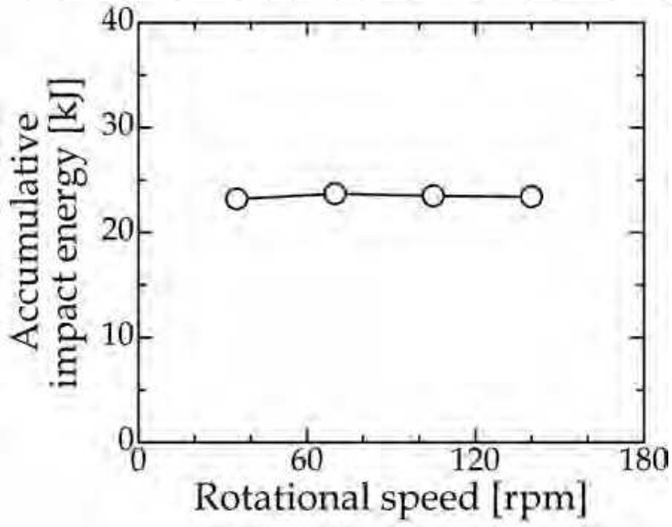

Fig. 18. Variation in accumulative impact energy required for completing Fe_3O_4 formation reaction with rotational speed.

In general mechanochemical processes, when the mechanical energy caused by shear, compression and friction actions of balls applies to particulate materials under dry condition, the surface energy of particles can increase due to the physical change such as distortion of the crystal lattice, increase of the surface area, and appearance of newly formed crystal surface. This causes the mechanochemical activation of particles. Under wet condition, however, the particles are difficult to undergo the mechanochemical activation because the increased surface energy is reduced by the solvent. Furthermore, it is very difficult to apply the mechanical energy effectively to nanoparticles. Accordingly, in this synthesis process, the mechanochemical activation of nanoparticles is difficult to occur, and the solid phase reaction from α-FeOOH to Fe_3O_4 may hardly proceed by direct contribution of the mechanical energy. However, at the rotational speed of 35 rpm, i.e. in a low mechanical energy field, the Fe_3O_4 formation reaction surely proceeded while the reaction rate was relatively low. There is no doubt that the applied mechanical energy promotes the reaction; the reaction mechanism in this synthesis process is considered that the reaction may proceed not by the mechanochemical activation of α-FeOOH but by local and rapid heating and/or through a different reaction path. In the conventional methods

for synthesizing Fe_3O_4 nanoparticles in water system, for promoting the formation reaction and increasing the crystallinity, the starting suspension in the vessel is heated from the outside by conductive heat transfer, resulting in temperature rise of the whole system. The heating is continued to keep the reaction temperature. This causes aggregation of the precipitates, leading to the growth of Fe_3O_4 nanoparticles. On the contrary, in the synthesis process with the ball-milling treatment, the suspension may be heated in the contact points between balls, which are extremely small regions, and then is cooled immediately because the pot and the balls are cooled enough. Therefore, local temperature rise of the suspension occurs instantaneously, and the heat energy is hardly stored in the system. In addition, the contact points exist discretely in the pot; the discrete heating occurs everywhere. Consequently, the heating type in the synthesis process is the internal heating, which is regarded as a non-uniform heating from a microscopic viewpoint but a uniform heating from a macroscopic one. This inhibits aggregation of the precipitates effectively, and the nucleation frequently occurs rather than the particle growth, resulting in the formation of the ultrafine Fe_3O_4 nanoparticles with high crystallinity and relatively narrow size distribution. Even at low rotational speeds, the Fe_3O_4 nanoparticles with a size of about 10 nm can be formed; this means that the aggregation-inhibition effect is confirmed in low energy fields.

4. Conclusion

A novel process for preparing superparamagnetic Fe_3O_4 nanoparticles with high crystallinity in water system has been developed, in which a cooled tumbling ball mill is used as the reaction field. It has been confirmed that this method provides successfully the Fe_3O_4 nanoparticles having a size of less than 15 nm without using any conventional heating techniques. This mechanochemical process was kinetically analyzed, indicating that the Fe_3O_4 formation reaction obeys the 0.6th-order rate equation. In addition, the mechanical energy (i.e., the impact energy of balls) promoting the Fe_3O_4 formation reaction was also analyzed using the numerical simulation method. The rate constant of the reaction was investigated based on the mechanical energy. As a result, the apparent activation energy of the reaction was estimated. This mechanochemical process may contribute to the production of superparamagnetic Fe_3O_4 nanoparticles under environmentally friendly conditions and be applied to another reaction systems synthesizing functional nanoparticles.

5. References

Buxbaum, G. & Pfaff, G. (2005). *Industrial Inorganic Pigments.* Third edition, Wiley-Vch, ISBN 978-3527303632, Weinheim, Germany.

Buyukhatipoglu, K.; Miller, T.A. & Morss Clyne, A. (2009). Flame synthesis and in vitro biocompatibility assessment of superparamagnetic iron oxide nanoparticles: Cellular uptake, toxicity and proliferation studies. *J. Nanosci. Nanotechnol.*, 9, 6834–6843.

Can, K.; Ozmen, M. & Ersoz, M. (2009). Immobilization of albumin on aminosilane modified superparamagnetic magnetite nanoparticles and its characterization. *Colloids Surf. B*, 71, 154–159.

Cheng, F.-Y.; Su, C.-H.; Yang, Y.-S.; Yeh, C.-S.; Tsai, C.-Y.; Wu, C.-L.; Wu, M.-T. & Shieh, D.-B. (2005). Characterization of aqueous dispersions of Fe_3O_4 nanoparticles and their biomedical applications. *Biomater.*, 26, 729–738.

Compeán-Jasso, M.E.; Ruiz, F.; Martínez, J.R. & Herrera-Gómez, A. (2008). Magnetic properties of magnetite nanoparticles synthesized by forced hydrolysis. *Mater. Lett.*, 62, 4248–4250.

Cundall, P.A. & Strack, O.D.L. (1979). A discrete numerical model for granular assemblies. *Geotechnique*, 29, 47–65.

Gao, F.; Cai, Y.; Zhou, J.; Xie, X.; Ouyang, W.; Zhang, Y.; Wang, X.; Zhang, X.; Wang, X.; Zhao, L. & Tang, J. (2010). Pullulan acetate coated magnetite nanoparticles for hyper-thermia: Preparation, characterization and in vitro experiments. *Nano Res.*, 3, 23–31.

Ge, J.; Hu, Y.; Biasini, M.; Beyermann, W.P. & Yin, Y. (2007). Superparamagnetic magnetite colloidal nanocrystal clusters. *Angew. Chem. Int. Ed.*, 46, 4342–4345.

Gudin, D.; Kano, J. & Saito, F. (2007). Effect of the friction coefficient in the discrete element method simulation on media motion in a wet bead mill. *Adv. Powder Technol.*, 18, 555–565.

Guo, S.; Li, D.; Zhang, L.; Li, J. & Wang, E. (2009). Monodisperse mesoporous superparamagnetic single-crystal magnetite nanoparticles for drug delivery. *Biomater.*, 30, 1881–1889.

Hakata, T. (2002). A novel composite carrier for electrophotographic developers. *J. Imaging Sci. Techn.*, 46, 591–597.

Hu, F.; MacRenaris, K.W.; Waters, E.A.; Schultz-Sikma, E.A.; Eckermann, A.L. & Meade, T.J. (2010). Highly dispersible, superparamagnetic magnetite nanoflowers for magnetic resonance imaging. *Chem. Commun.*, 46, 73–75.

Hua, C.C.; Zakaria, S.; Farahiyan, R.; Khong, L.T.; Nguyen, K.L.; Abdullah, M. & Ahmad, S. (2008). Size-controlled synthesis and characterization of Fe_3O_4 nanoparticles by chemical coprecipitation method. *Sains Malays.*, 37, 389–394.

Iwasaki, T.; Kosaka, K.; Mizutani, N.; Watano, S.; Yanagida, T.; Tanaka, H. & Kawai, T. (2008). Mechanochemical preparation of magnetite nanoparticles by coprecipitation. *Mater. Lett.*, 62, 4155–4157.

Iwasaki, T.; Kosaka, K.; Yabuuchi, T.; Watano, S.; Yanagida, T. & Kawai, T. (2009). Novel mechanochemical process for synthesis of magnetite nanoparticles using coprecipitation method. *Adv. Powder Technol.*, 20, 521–528.

Iwasaki, T.; Kosaka, K.; Watano, S.; Yanagida, T. & Kawai, T. (2010). Novel environmentally friendly synthesis of superparamagnetic magnetite nanoparticles using mechanochemical effect. *Mater. Res. Bull.*, 45, 481–485.

Iwasaki, T.; Mizutani, N.; Watano, S.; Yanagida, T. & Kawai, T. (2011a). Size control of magnetite nanoparticles by organic solvent-free chemical coprecipitation at room temperature. *J. Exp. Nanosci.*, in press.

Iwasaki, T.; Sato, N.; Kosaka, K.; Watano, S.; Yanagida, T. & Kawai, T. (2011b). Direct transformation from goethite to magnetite nanoparticles by mechanochemical reduction. *J. Alloys Compd.*, 509, L34–L37.

Kano, J.; Mio, H. & Saito, F. (2000). Correlation of grinding rate of gibbsite with impact energy of balls. *AIChE J.*, 46, 1694–1697.

Lee, C.M.; Jeong, H.J.; Kim, E.M.; Kim, D.W.; Lim, S.T.; Kim, H.T.; Park, I.K.; Jeong, Y.Y.; Kim, J.W. & Sohn, M.H. (2009). Superparamagnetic iron oxide nanoparticles as a dual imaging probe for targeting hepatocytes in vivo. *Magn. Reson. Med.*, 62, 1440–1446.

Lee, J.; Isobe, T. & Senna, M. (1996). Magnetic properties of ultrafine magnetite particles and their slurries prepared via in-situ precipitation. *Colloids Surf. A*, 109, 121–127.

Li, Y.G.; Gao, H.S.; Li, W.L.; Xing, J.M. & Liu, H.Z. (2009). In situ magnetic separation and immobilization of dibenzothiophene-desulfurizing bacteria. *Bioresource Technol.*, 100, 5092–5096.

Lian, S.; Wang, E.; Kang, Z.; Bai, Y.; Gao, L.; Jiang, M.; Hu, C. & Xu, L. (2004). Synthesis of magnetite nanorods and porous hematite nanorods. *Solid State Commun.*, 129, 485–490.

Mizutani, N.; Iwasaki, T.; Watano, S.; Yanagida, T.; Tanaka, H. & Kawai, T. (2008). Effect of the ferrous/ferric ions molar ratio on the reaction mechanism for the hydrothermal synthesis of magnetite nanoparticles. *Bull. Mater. Sci.*, 31, 713–717.

Mizutani, N.; Iwasaki, T.; Watano, S.; Yanagida, T. & Kawai, T. (2010). Size control of magnetite nanoparticles in hydrothermal synthesis by coexistence of lactate and sulfate ions. *Curr. Appl. Phys.*, 10, 801–806.

Muzquiz-Ramos, E.M.; Cortes-Hernandez, D.A. & Escobedo-Bocardo, J. (2010). Biomimetic apatite coating on magnetite particles. *Mater. Lett.*, 64, 1117–1119.

Ochiai, M.; Masui, M.; Asanae, M.; Tokunaga, M. & Iimura, T. (1994). Magnetic toner prepared by the suspension polymerization method. *J. Imaging Sci. Techn.*, 38, 415–420.

Tsuji, Y.; Tanaka, T. & Ishida, T. (1992). Lagrangian numerical simulation of plug flow of cohesionless particles in a horizontal pipe. *Powder Technol.*, 71, 239–250.

Wan, J.; Tang, G. & Qian, Y. (2007). Room temperature synthesis of single-crystal Fe_3O_4 nanoparticles with superparamagnetic property. *Appl. Phys. A*, 86, 261–264.

Wang, S.; Bao, H.; Yang, P. & Chen, G. (2008). Immobilization of trypsin in polyaniline-coated nano-Fe_3O_4/carbon nanotube composite for protein digestion. *Anal. Chim. Acta*, 612, 182–189.

Wen, X.; Yang, J.; He, B. & Gu, Z. (2008). Preparation of monodisperse magnetite nanoparticles under mild conditions. *Curr. Appl. Phys.*, 8, 535–541.

Wu, J.-H.; Ko, S.P.; Liu, H.-L.; Kim, S.; Ju, J.-S. & Kim, Y.K. (2007). Sub 5 nm magnetite nanoparticles: Synthesis, microstructure, and magnetic properties. *Mater. Lett.*, 61, 3124–3129.

Wu, J.H.; Ko, S.P.; Liu, H.L.; Jung, M.-H.; Lee, J.H.; Ju, J.-S. & Kim, Y.K. (2008). Sub 5 nm Fe_3O_4 nanocrystals via coprecipitation method. *Colloids Surf. A*, 313-314, 268–272.

Yu, S.; Wan, J.; Yu, X. & Chen, K. (2010). Preparation and characterization of hydrophobic magnetite microspheres by a simple solvothermal method. *J. Phys. Chem. Solids*, 71, 412–415.

Yang, D.P.; Gao, F.; Cui, D.X. & Yang, M. (2009). Microwave rapid synthesis of nanoporous Fe_3O_4 magnetic microspheres. *Curr. Nanosci.*, 5, 485–488.

Zheng, Y.-H.; Cheng, Y.; Bao, F. & Wang, Y.-S. (2006). Synthesis and magnetic properties of Fe_3O_4 nanoparticles. *Mater. Res. Bull.*, 41, 525–529.

Zhou, L.; Yuan, J.; Yuan, W.; Zhou, M.; Wu, S.; Li, Z.; Xing, X. & Shen, D. (2009). Synthesis and characterization of multi-functional hybrid magnetite nanoparticles with biodegradability, superparamagnetism, and fluorescence. *Mater. Lett.*, 63, 1567–1570.

Materials Science and Technology

Edited by Prof. Sabar Hutagalung

ISBN 978-953-51-0193-2
Hard cover, 324 pages
Publisher InTech
Published online 07, March, 2012
Published in print edition March, 2012

Materials are important to mankind because of the benefits that can be derived from the manipulation of their properties, for example electrical conductivity, dielectric constant, magnetization, optical transmittance, strength and toughness. Materials science is a broad field and can be considered to be an interdisciplinary area. Included within it are the studies of the structure and properties of any material, the creation of new types of materials, and the manipulation of a material's properties to suit the needs of a specific application. The contributors of the chapters in this book have various areas of expertise. therefore this book is interdisciplinary and is written for readers with backgrounds in physical science. The book consists of fourteen chapters that have been divided into four sections. Section one includes five chapters on advanced materials and processing. Section two includes two chapters on bio-materials which deal with the preparation and modification of new types of bio-materials. Section three consists of three chapters on nanomaterials, specifically the study of carbon nanotubes, nano-machining, and nanoparticles. Section four includes four chapters on optical materials.

InTech Europe
University Campus STeP Ri
Slavka Krautzeka 83/A
51000 Rijeka, Croatia
Phone: +385 (51) 770 447
Fax: +385 (51) 686 166
www.intechopen.com

InTech China
Unit 405, Office Block, Hotel Equatorial Shanghai
No.65, Yan An Road (West), Shanghai, 200040, China
中国上海市延安西路65号上海国际贵都大饭店办公楼405单元
Phone: +86-21-62489820
Fax: +86-21-62489821

IntechOpen